Int. J. Heat Mass Transfer. Vol. 36, No. 14, pp. 3459–3475, 1993
Printed in Great Britain

0017–9310/93 $6.00+0.00

Computational modeling of the gas-phase transport phenomena during flame-jet thermal spallation drilling

MARK A. WILKINSON and JEFFERSON W. TESTER
Chemical Engineering Department and Energy Laboratory, MA Institute of Technology, Cambridge, Massachusetts 02139, U.S.A.

(*Received* 29 *June* 1992 *and in final form* 10 *February* 1993)

Abstract—Rock spallation induced by thermal stress can be used to drill through hard rock at high rates. In order to characterize the importance of operating parameters on rock penetration rate and hole geometry, a modeling effort was initiated. Because supersonic flame jets are used to induce thermal stress in practical spallation drilling systems, a comprehensive treatment of turbulent gas phase heat, mass, and momentum transport was developed and coupled to a rock mechanics-based model of thermal stress induced failure. Work reported in this paper provides the mathematical framework, governing equations, and computational algorithms and compares model-predicted results to experimental data when possible.

1. INTRODUCTION

THERMAL spallation can be broadly defined as fragmentation of the surface of a brittle solid into small disk-like flakes, called spalls, by rapidly heating a relatively small fraction of the solid (e.g. less than 10% of the exposed area). Thermal stresses arising from the tendency of the heated portion of the material to expand as temperature is increased cause failure to occur. When thermal spallation is used for rock drilling, a 'flame-jet' like the one shown in Fig. 1 is commonly used to impart the high heat fluxes (typically greater than 1.0 MW m^{-2}) required and to sweep away the spalls [1, 2]. Typically, the gas flow exiting a flame-jet is underexpanded at a nozzle-to-ambient pressure ratio of at least 4.4. The high jet momentum sweeps spalls away from the rock surface rapidly, exposing new surface area for further penetration.

Drilling systems that employ conventional rotary methods that crush and grind rock with hardened tricone bits are inherently prone to wear and failure, especially when encountering hard rock in deep formations. These and other factors give rise to an exponential or near-exponential dependence of drilling costs on depth [3, 4]. Flame-jet methods operate with a fundamentally different mechanism of rock failure, so that it may be possible to reduce substantially this exponential dependence of drilling costs on depth. Initial applications of thermal spallation drilling technology are envisioned for developing the so-called hot dry rock geothermal resource in hard, crystalline rock. In regions with low geothermal gradients, deep (>5 km) holes would be needed [3, 4]. Now, however, it appears that the market for spallation applications may be expanding to oil and gas development as a recent breakthrough has been reported where limestone has been successfully spalled using a flame-jet device [5].

Earlier research on spallation at MIT by Rauenzahn [6] and Rauenzahn and Tester [7–10] established the basis for the present study. In the current phase of our research, we have focused on further characterization of fundamental mechanisms of spall formation and on modeling fluid flow and heat transfer processes important to simulating drilling and quarrying conditions observed in practice [2, 11]. A key objective was predicting penetration rate and borehole geometry as a function of primary operating variables such as flame temperature, jet velocity, nozzle standoff distance, and the thermophysical properties of the

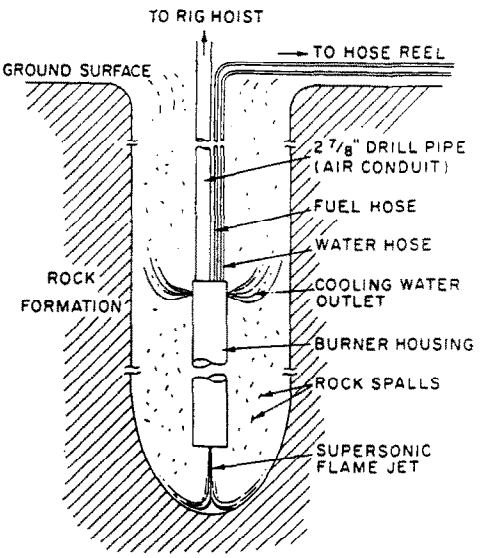

FIG. 1. Schematic of thermal spallation drilling [2].

NOMENCLATURE

a speed of sound [m s^{-1}]
CFL non-dimensional timestep, $a\Delta t/\Delta x$
C_L spall diameter : thickness ratio
C_p constant pressure heat capacity [J kg^{-1} K^{-1}]
C_μ universal turbulent viscosity constant (0.09)
$\mathbf{D}^n$ artificial dissipation after the nth stage
E total energy [J]
E_M Young's modulus [MPa]
$\mathbf{F}$ convective radial flux vector
$\mathbf{G}$ convective axial flux vector
ΔH_{pt} energy losses due to miscellaneous phase transitions and crack formation [W m^{-2}]
I internal energy [J]
J Jacobian
k turbulent kinetic energy
k_r rock thermal conductivity [W m^{-1} K^{-1}]
$\mathbf{L}$ unweighted Laplacian operator
$\bar{\mathbf{L}}$ modified Laplacian operator (equation (29))
m Weibull homogeneity parameter
$\mathbf{M}$ source term vector
Ma_{jet} jet Mach number, U_{jet}/a_{jet}
P pressure [Pa]
P_k production rate of turbulent kinetic energy
P_ε production rate of dissipation of turbulent kinetic energy
Pr_t turbulent Prandtl number (0.86)
$\dot{q}_i$ heat flux in direction i [W m^{-2}]
Q_r local heat flux to rock [W m^{-2}]
Q_p predicted heat flux [W m^{-2}]
Q_{jet} total jet inlet enthalpy flux [W m^{-2}]
Q_w wall heat flux [W m^{-2}]
r radial coordinate direction [m]
R ideal gas constant, 8.314 J mol^{-1} K^{-1}
R_{pr} average non-dimensional penetration rate (equation (41))
$\mathbf{R}$ radial viscous flux vector
Re_{jet} nozzle Reynolds number, $\rho_{jet}U_{jet}R_{noz}/\mu_{jet}$
R_{noz} nozzle radius [m]
R_h hole radius [m]
$\mathbf{R}^k$ residual representing spatially discretized terms in equation (16)
$\mathbf{S}$ axial viscous flux vector
SOD dimensionless stand-off distance, Z_{dr}/R_{noz}
St Stanton number
St_p Stanton number based on predicted surface heat flux
St_{exp} Stanton number based on experimentally measured penetration rate
t time [s]
T temperature [K]
T_s local surface temperature [K]
T_{r0} initial rock temperature [K]
$T_{s,st}$ stagnation point surface temperature [K]
T_{jet} gas temperature at nozzle outlet [K]
u radial velocity component [m s^{-1}]
$\mathbf{U}$ state vector $(\rho, \rho u, \rho v, \rho E)$
U_{dr} local drilling velocity normal to rock surface [m s^{-1}]
U_{jet} jet velocity [m s^{-1}]
v axial velocity component [m s^{-1}]
V sample or cell volume [m^3]
$\mathbf{V}$ velocity vector (u, v) [m s^{-1}]
V_{dr} forward drilling or penetration rate [m s^{-1}]
y distance measured in a direction perpendicular to the rock wall [m]
z axial coordinate direction; distance measured normal to rock surface [m]
Z_{dr} axial distance from the stagnation point to the nozzle outlet [m].

Greek symbols

α_r thermal diffusivity of the rock [m^2 s^{-1}]
β_r thermal coefficient of expansion, $V^{-1}(\partial V/\partial T)_p$ [K^{-1}]
γ heat capacity ratio, C_p/C_v
δ_{ij} Kronecker delta (1 if $i = j$; 0 if $i \neq j$)
ε turbulent dissipation rate of turbulent kinetic energy
$\varepsilon_2, \varepsilon_4$ 2nd and 4th difference artificial viscosity coefficients
θ angle between tangent to the rock surface and the horizontal axis; coordinate direction
κ von Karman turbulence constant (0.41)
λ thermal conductivity [W m^{-1} K^{-1}]
μ dynamic viscosity [kg^{-1} m^{-1} s^{-1}]
ν_p Poisson's ratio
ξ horizontal axis coordinate in 2-D computational space
ρ density [kg m^{-3}]
σ stress [MPa]
τ_{ij} deviatoric stress component in the i, j direction [Pa]
η vertical axis coordinate in 2-D computational space
ω boundary movement acceleration parameter.

Subscripts and superscripts

bl boundary layer edge property
dr drill
exp experimental value
ε relevant to turbulent dissipation rate equation
f cell face property

jet	at jet outlet (nozzle)	r	rock property
k	relevant to turbulent kinetic energy equation	s	rock surface property
		sp	at spallation
loc	local conditions	st	at stagnation point conditions
max	maximum	t	turbulent conditions
noz	at nozzle	T	total
pr	penetration rate	w	wall conditions (in gas phase).

rock. As discussed in the following section, the heat flux and surface temperature on a spalling surface determine the penetration or drilling rate in a specific rock type. A distribution of heat fluxes and rock surface temperatures leads to a range of drilling velocities and thereby determines the hole shape and the net forward drilling rate.

Rauenzahn and Tester [9, 10] developed a method for predicting rock surface heat fluxes and surface temperatures using a computational model of the fluid mechanics and heat transfer from a flame jet to a spalling rock surface and using Dey's [12] rock mechanics based thermal spallation model. The present study was aimed at improving the accuracy of heat flux predictions over a practical range of operating parameters. Experimental validation of some results are described in detail in a separate paper (Wilkinson and Tester [13]).

In this paper, we first present the equations governing thermal spallation drilling and then provide the details of our approach to modeling fluid mechanics and heat transfer processes, including the numerical method used to solve the conservation equations. Validation studies, grid generation methodology, and the numerical algorithm used to calculate the position of the rock boundary during the simulation are then described briefly. Comparisons of computational and experimental results are discussed in the final sections of the paper.

2. EQUATIONS GOVERNING STEADY-STATE THERMAL SPALLATION DRILLING

A local energy balance on a control volume surrounding the rock–gas interface during thermal spallation drilling may be written as:

$$Q = (\rho_r C_{pr}) U_{dr} (T_s - T_{r0}) + \Delta H_{pt} \qquad (1)$$

where ρ_r = rock density [kg m^{-3}], C_{pr} = rock heat capacity at constant pressure [J kg^{-1} K^{-1}], Q = local heat flux to the rock [W m^{-2}], U_{dr} = local penetration rate normal to the surface [m s^{-1}], ΔH_{pt} = energy losses due to miscellaneous phase transitions and crack formation [W m^{-2}], T_s = local surface temperature [K], and T_{r0} = initial rock temperature [K]. Equation (1) is derived assuming quasi-steady state conditions and that the entire spall is approximately at the surface temperature of the rock [6]. The second term on the right-hand side of equation (1) (ΔH_{pt}) is expected to be negligible during thermal spallation drilling, except near the rock melting temperature.

Assuming that steady-state flame-jet thermal spallation drilling is possible, the average hole shape in the actively spalling region must remain constant and satisfy the condition that the forward component of the local penetration rate is the same everywhere. This is illustrated in Fig. 2 and can be expressed mathematically as:

$$V_{dr} = \frac{U_{dr}}{\cos(\theta)} \qquad (2)$$

where V_{dr} = forward advance rate of drill head [m s^{-1}], and θ = angle of the tangent of the rock

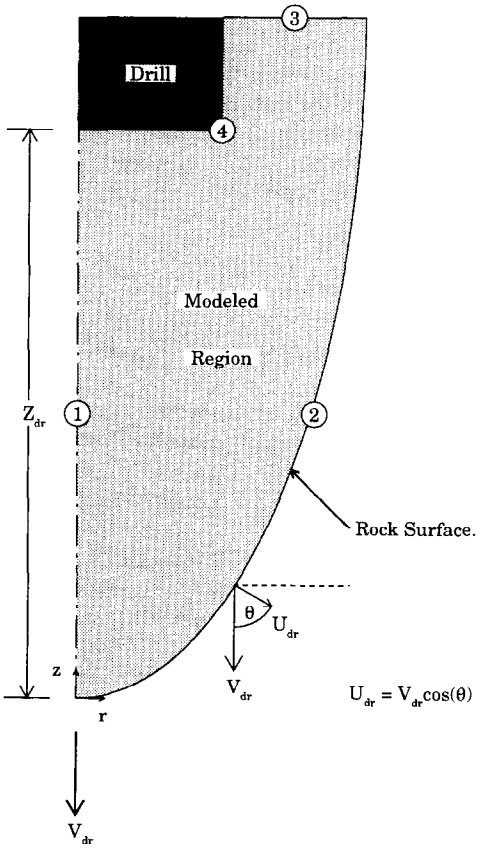

FIG. 2. Illustration of modeled region and self-consistency condition (equation (2)).

boundary to the horizontal plane. One can easily show by simple geometric reasoning that θ is also equivalent to the angle between the normal to the rock boundary and the vertical plane as shown in Fig. 2.

Heat flux and hole diameter predictions are compared with experimental results by forming non-dimensional Stanton numbers and hole radii. In this case, the Stanton number (St) is defined as the ratio of the rock surface heat flux (Q_r) to the total jet inlet heat flux (Q_{jet}), or:

$$St = Q_r/Q_{jet} \tag{3}$$

where

$$Q_{jet} = (\rho C_p U)_{jet}(T_{jet} - T_s)$$

and T_{jet} is the gas temperature at the nozzle outlet. In order to determine an experimental value of the Stanton number (St_{exp}) from a measured penetration rate (V_{dr}), Q_r is calculated from equation (1) giving:

$$St_{exp} = \frac{(\rho C_p)_r V_{dr}(T_s - T_{r0})}{(\rho C_p U)_{jet}(T_{jet} - T_s)}. \tag{4}$$

Computer simulation results predict directly the rock surface heat flux so that predicted Stanton number (St_p) is given as a function of predicted heat flux (Q_p):

$$St_p = \frac{Q_p}{(\rho C_p U)_{jet}(T_{jet} - T_s)}. \tag{5}$$

The final requirement for estimating drilling rate and hole shape during thermal spallation drilling is a functional relationship between the rock surface temperature and the applied heat flux. Using Dey's [12] thermal spallation rock mechanics model based on a failure mechanism characterized by Weibull statistics, the surface temperature is given by:

$$T_s = T_{r0} + \left[\left(\frac{Q_r}{(\rho C_p)_r}\right)^3 \left[\frac{(1-\nu_p)\sigma_o}{\beta_r E_M}\right]^m \times \left(\frac{2(0.693)}{\pi C_L^2}\right)\left(\frac{m}{\alpha_r}\right)^3\right]^{1/(m+3)} \tag{6}$$

where the spall diameter to thickness ratio $C_L = 15$, m and σ_o represent empirically-fitted Weibull parameters, ν_p = Poisson's ratio, β_r = coefficient of thermal expansion, E_m = Young's modulus, and α_r = thermal diffusivity.

Rauenzahn and Tester [9] used Dey's model and semi-empirical fitting parameters estimated from mechanical spallation tests conducted at ambient temperature. In an earlier paper [13], Wilkinson and Tester estimated that errors resulting from the use of mechanically-based Weibull parameters probably accounted for about 50% of the discrepancy between predictions and experimental measurements reported earlier [9, 10]. Furthermore, we derived more accurate fitting parameters based on surface temperature measurements and estimates of the heat flux occurring during thermal spallation drilling.

3. PREDICTING THERMAL SPALLATION FORWARD DRILLING RATE AND HOLE DIAMETER: MODEL DEVELOPMENT

As discussed in the previous section, predicting forward drilling rate and hole diameter requires knowledge of the spatial distribution of rock surface temperature and heat flux. Determining the heat flux requires solution of the mass, momentum, and energy conservation equations for the high temperature gas stream that impinges on the spalling rock surface. The model development and numerical method used in the present study are described in this section.

Governing equations

The governing conservation equations for mass, momentum, and energy are solved subject to the appropriate boundary conditions and constitutive relationships. The equations are approximated on a finite grid of points. Estimated surface heat fluxes are used to re-position the simulated rock boundary until the hole shape conforms to the consistency criterion given by equation (2). The governing equations are expressed in axisymmetric, vector form as:

$$\frac{\partial \mathbf{U}}{\partial t} + \frac{1}{r}\frac{\partial r\mathbf{F}}{\partial r} + \frac{\partial \mathbf{G}}{\partial z} = \frac{1}{r}\frac{\partial r\mathbf{R}}{\partial r} + \frac{\partial \mathbf{S}}{\partial z} + \mathbf{M} \tag{7}$$

where:

$$\mathbf{U} = \begin{bmatrix} \rho \\ \rho u \\ \rho v \\ \rho E \end{bmatrix} \quad \mathbf{F} = \begin{bmatrix} \rho u \\ \rho u^2 + P \\ \rho uv \\ u(\rho E + P) \end{bmatrix}$$

$$\mathbf{G} = \begin{bmatrix} \rho v \\ \rho uv \\ \rho v^2 + P \\ v(\rho E + P) \end{bmatrix}$$

$$\mathbf{R} = \begin{bmatrix} 0 \\ \tau_{rr} \\ \tau_{rz} \\ u\tau_{rr} + v\tau_{rz} - \dot{q}_r \end{bmatrix} \quad \mathbf{S} = \begin{bmatrix} 0 \\ \tau_{rz} \\ \tau_{zz} \\ u\tau_{rz} + v\tau_{zz} - \dot{q}_z \end{bmatrix}$$

$$\mathbf{M} = \begin{bmatrix} 0 \\ \sigma_{\theta\theta}/r \\ 0 \\ 0 \end{bmatrix}$$

$$\tau_{rz} = \tau_{zr} = \mu\left(\frac{\partial u}{\partial z} + \frac{\partial v}{\partial r}\right)$$

$$\sigma_{\theta\theta} = P - \left(2\mu\frac{u}{r} - \tfrac{2}{3}\mu\,\mathrm{div}\,(\mathbf{V})\right)$$

$$\rho E = \left(\frac{P}{\gamma - 1}\right) + \tfrac{1}{2}\rho(\mathbf{V}\cdot\mathbf{V})$$

$$\mathrm{div}\,(\mathbf{V}) = \frac{1}{r}\frac{\partial ru}{\partial r} + \frac{\partial v}{\partial z}$$

$\mathbf{V}$ = velocity vector with radial (u) and axial (v) components, $\tau_{i,j}$ = deviatoric stress tensor component in the i,j direction [Pa], u, v = radial and axial velocity components [m s^{-1}], r, z = radial and axial coordinates [m], E = total energy per unit mass [J kg^{-1}], γ = ratio of heat capacities, C_p/C_v, and P = fluid pressure [N m^{-2}].

The set of equations employed in this study and expressed by equation (7) are the 'Reynolds averaged' conservation equations [14]. These equations include the effects of turbulent momentum and heat transport and therefore contain additional components in the stress tensor and in the heat flux vector due to turbulent fluctuation (see ref. [31] for details).

In the present study, the flow-field is conceptually divided into a near wall region, where hydrodynamic behavior is similar to that in a compressible turbulent flat-plate boundary layer, and a far-field, where simple models based upon well-known velocity and temperature profiles cannot be used. In the far-field region, the k–ε turbulence model described by Launder and Spalding [16] is used to calculate the turbulent viscosity coefficient according to the following relationship, obtained from scaling arguments applied to the transport equation for turbulent kinetic energy:

$$\mu_t = \frac{\rho C_\mu k^2}{\varepsilon} \tag{8}$$

where k is the turbulent kinetic energy per unit mass, and ε is the isotropic dissipation rate of turbulent kinetic energy per unit mass. The value of C_μ has been experimentally determined to equal 0.09 [17].

When using the k–ε turbulence model, transport equations are written for k and ε as functions of mean flow-field properties. These equations have been derived from the turbulent form of the conservation of momentum equation. The final modeled turbulent kinetic energy and dissipation rate equations used in the present study are [18]:

$$\frac{\partial \rho k}{\partial t} = -\left(\frac{1}{r}\frac{\partial(r\rho u k)}{\partial r} + \frac{\partial(\rho v k)}{\partial z}\right) + \left(\frac{1}{r}\frac{\partial(r\mu_k \partial k/\partial r)}{\partial r} + \frac{\partial(\mu_k \partial k/\partial z)}{\partial z}\right) + P_k - \rho\varepsilon \tag{9}$$

$$\frac{\partial \rho \varepsilon}{\partial t} = -\left(\frac{1}{r}\frac{\partial(r\rho u \varepsilon)}{\partial r} + \frac{\partial(\rho v \varepsilon)}{\partial z}\right) + \left(\frac{1}{r}\frac{\partial(r\mu_\varepsilon \, \mathrm{d}\varepsilon/\partial r)}{\partial r} + \frac{(\mu_\varepsilon \partial \varepsilon/\partial z)}{\partial z}\right) + \frac{\varepsilon}{k}(C_1 P_\varepsilon - C_2 \rho\varepsilon) \tag{10}$$

where P_k and P_ε are the rate of production of turbulent kinetic energy, and the rate of production of dissipation of turbulent kinetic energy, respectively:

$$P_k = \frac{\mu_t}{\mu_T}\left[\tau_{rr}\left(\frac{\partial u}{\partial r}\right) + \tau_{rz}\left(\frac{\partial u}{\partial z} + \frac{\partial v}{\partial r}\right) + \tau_{zz}\left(\frac{\partial v}{\partial z}\right) - \frac{\tau_{\theta\theta} u}{r}\right] - \tfrac{2}{3}\mathrm{div}\,(\mathbf{V}) \tag{11}$$

$$P_\varepsilon = \frac{\mu_t}{\mu_T}\left[C_3\tau_{rr}\left(\frac{\partial u}{\partial r}\right) + \tau_{rz}\left(\frac{\partial u}{\partial z} + \frac{\partial v}{\partial r}\right) + C_3\tau_{zz}\left(\frac{\partial v}{\partial z}\right) - C_3\frac{\tau_{\theta\theta} u}{r}\right] - \tfrac{2}{3}C_3\,\mathrm{div}\,(\mathbf{V}) \tag{12}$$

where μ_k, μ_ε = turbulent diffusion coefficients for k and ε, $C_1 = 1.55$, $C_2 = 2.0$, $C_3 = 1.0$, and $\mu_T = \mu_t + \mu$.

These equations are solved throughout the designated 'far-field' domain in order to be able to ultimately calculate the wall-region heat transfer. A modified form of the semi-theoretical Prandtl [19] mixing length model is used in the near-wall region for predicting velocity and temperature profiles. The final expressions for the wall shear stress (τ_w) and heat flux (Q_w) are:

$$\tau_w = \frac{\rho_w u_p \theta C_\mu^{1/4}\sqrt{k}}{\frac{1}{\kappa}\ln\left(32.6\frac{y^+}{h^+} + 1\right)} \tag{13}$$

$$Q_w = \frac{[C_p(T_p - T_w) + \frac{1}{2}u^2]\rho_w \theta C_\mu^{1/4}\sqrt{k}}{\frac{Pr_t}{\kappa}\ln\left(32.6\frac{y^+}{h^+} + 1\right) + St_{rh}^{-1}}$$

$$\theta = \int_0^1 \left[\left(\frac{\rho}{\rho_p}\right)^{1/2} d\left(\frac{u^+}{u_p^+}\right)\right];$$

$$St_{rh}^{-1} = \frac{(T_{rh} - T_w)}{\left(\frac{Q_w}{(\rho_w C_p)}\right)}\left(\frac{\tau_w}{\rho_w}\right)^{1/2} \tag{14}$$

where T_{rh} = temperature at the outer edge of the surface roughness, $h^+ = hu_\tau\rho/\mu$, h = r.m.s. surface roughness height, κ = von Karman constant (0.41), Pr_t = turbulent Prandtl number $\cong 0.86$, $u_\tau = (\tau_w/\rho_w)^{1/2}$, and $St_{rh}^{-1} = 5.19\, h^{+0.20}\, Pr^{0.44}$ [20].

Boundary conditions

The boundary conditions that are used to solve the conservation equations (7) are depicted on Fig. 3. The centerline boundary is assumed to be an axis of symmetry and therefore represents a zero flux condition. Solid walls, for example the spalling rock surface, are treated as no slip boundaries with zero pressure gradients normal to the surface. Temperature is specified on the rock surface from equation (6), whereas the drill housing was assumed to be adiabatic. Physical properties and Weibull parameters, m and σ_0, are averages of Barre and Westerly granite values (see ref. [13]). The turbulent kinetic energy is set equal to zero on solid surfaces, and the dissipation rate is specified at the computational node nearest to the wall by the following relationship [16]:

$$\varepsilon = \frac{C_\mu k^{3/2}}{y_p}. \tag{15}$$

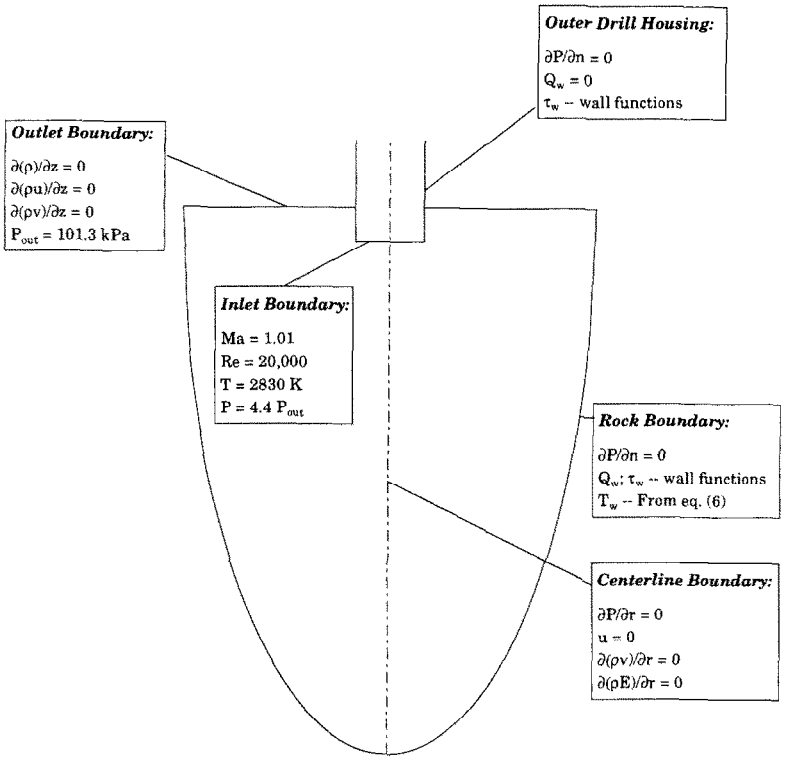

FIG. 3. Boundary conditions.

At the nozzle outlet, the turbulent kinetic energy is specified as 5% of the mean flow kinetic energy and the turbulent length scale is specified as one-third of the nozzle radius. At the outlet from the cavity, zero streamwise gradients are assumed for all variables except pressure. Pressure is set from the user-defined under-expansion ratio (P_{noz}/P_{amb}) which equals 4.4 for all cases tested.

Solution of governing equations

Discretization techniques are adopted whereby the property conservation laws are expressed for small (but finite) volume elements that are formed by breaking up the flow-field domain into a grid of points. The net flux of mass, momentum, and energy into each volume element (or 'cell') is approximated and numerical time integration is performed until all cells are at steady-state conditions (no accumulation).

A finite volume approach described in detail by Wilkinson [21] was used to formulate the discrete set of conservation equations giving:

$$V\frac{\partial \mathbf{U}}{\partial t}+\oint[(r\mathbf{F}_2)\partial z-(r\mathbf{G})\partial r]-\oint[(r\mathbf{R})\partial z-(r\mathbf{S})\partial r]$$

(I) (II) (III)

$$+\oint\oint\frac{\partial \mathbf{P}}{\partial r}r\mathrm{d}r\mathrm{d}z=V\mathbf{M}_2$$

(IV) (V) (16)

where

$$V \equiv \text{cell volume}$$

$$\mathbf{M}_2 \equiv 1/(Re_r[0, -\tau_{\theta\theta}/r, 0, 0]$$

$$\mathbf{F}_2 \equiv \mathbf{F}-[0, P, 0, 0].$$

Equation (16) serves as a starting point for discretizing the flow-field and approximating the flux balances. The first term on the left hand side of equation (16) represents the rate of change of the state vector inside a given spatial region having a volume V. The second and third terms are convective and diffusive flux balances that effectively sum all inflows and outflows of conserved quantities from the volume. The pressure integral to the left of the '=' sign and the source term appearing on the right hand side of the equation arise from the use of an axisymmetric co-ordinate system. The following sections give details of the method used for solving equation (16) in the physical domain applicable to spallation drilling.

4. FLUX CALCULATIONS

The line integrals appearing in equation (16) are rewritten in terms of face integrals on each edge of the computational cell (see Fig. 4(a)) and then the fluxes are approximated. For example, the convective flux integral is written

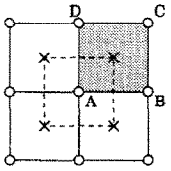

a) Convective Flux Cell (shaded).

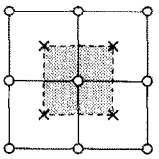

b) Node Cell -- Viscous Flux Balance.

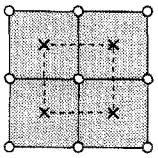

c) Node Super Cell -- Total Flux Balance.

FIG. 4. Integration areas for convective, viscous or diffusive and total flux balances.

$$\oint_A^D [(r\mathbf{F}_2)\partial z-(r\mathbf{G})\partial r] = \oint_A^B [(r\mathbf{F}_2)\partial z-(r\mathbf{G})\partial r] + \oint_B^C [(r\mathbf{F}_2)\partial z-(r\mathbf{G})\partial r] + \oint_C^D [(r\mathbf{F}_2)\partial z-(r\mathbf{G})\partial r] + \oint_D^A [(r\mathbf{F}_2)\partial z-(r\mathbf{G})\partial r]. \quad (17)$$

Each of these integrals is approximated by assuming that r, z, $\mathbf{F}_2$, and $\mathbf{G}$ vary linearly along the cell faces [22]. For face A-B this gives:

$$r = r_A(1-\xi)+r_B\xi,$$

$$\mathbf{F}_2 = \mathbf{F}_{2A}(1-\xi)+\mathbf{F}_{2B}\xi, \text{ etc.}\ldots.$$

where ξ varies linearly from zero to one with distance along the face. The integrated expression for the convective fluxes on face A-B is given by [22]

$$\oint_A^B [(r\mathbf{F}_2)\partial z-(r\mathbf{G})\partial r] = \left(\frac{r_B-r_A}{6}\right)[r_A(2\mathbf{F}_{2A}+\mathbf{F}_{2B})+r_B(2\mathbf{F}_{2B}+\mathbf{F}_{2A})] + \left(\frac{z_B-z_A}{6}\right)[z_A(2\mathbf{G}_A+\mathbf{G}_B)+r_B(2\mathbf{G}_B+\mathbf{G}_A)] \quad (18)$$

where $\mathbf{F}_{2A}$, and $\mathbf{G}_A$ are flux vectors evaluated at node point A. This formulation results in leading error magnitudes of $O(\Delta x^2)$ everywhere in the flow-field whereas a more commonly used and straightforward method of neglecting the variations of r in the face-integrals result in $O(\Delta x)$ or less accuracy near the axis of symmetry where $r \to 0$.

The fourth term (IV) in equation (16) is discretized using a pseudo finite-element technique in which the pressure derivative is expanded using the chain rule, leading to:

$$\frac{\partial P}{\partial r} = \frac{1}{|J|}\left(\frac{\partial P}{\partial \xi}\frac{\partial z}{\partial \eta}-\frac{\partial P}{\partial \eta}\frac{\partial z}{\partial \xi}\right) \quad (19)$$

where $|J|$ = Jacobian determinant, and ξ, η = local coordinates in computational space ($0 \leqslant \xi, \eta \leqslant 1$).

Radius and pressure variations on a cell are given by:

$$r = r_A(1-\xi)(1-\eta)+r_B(\xi)(1-\eta)+r_C(\xi)(\eta)+r_D(1-\xi)(\eta) \quad (20)$$

$$P = P_A(1-\xi)(1-\eta)+P_B(\xi)(1-\eta)+P_C(\xi)(\eta)+P_D(1-\xi)(\eta). \quad (21)$$

Substituting equations (20), (21), and (19) into term (IV) of equation (16) leads to [22]

$$\oiint r\frac{\partial P}{\partial r}\,dr\,dz = \frac{(z_B-z_D)}{24}[P_A(4r_A+3r_B+2r_C+3r_D) - P_A(2r_A+3r_B+4r_C+3r_D)] - \frac{(z_A-z_C)}{24}[P_B(3r_A+4r_B+3r_C+2r_D) - P_D(3r_A+2r_B+3r_C+4r_D)] + \frac{(r_B-r_D)}{24}[P_A(x_B+x_D-2x_C) - P_C(x_B+x_D-2x_A)] - \frac{(r_A-r_C)}{24}[P_B(x_A+x_C-2x_D) - P_D(x_A+x_C-2x_B)]. \quad (22)$$

Velocity and temperature derivatives are required for evaluating the viscous stresses and heat fluxes ($\mathbf{R}$ and $\mathbf{S}$) appearing in equation (16). Green's theorem is used to approximate each derivative as an integral around a cell, resulting in cell-centered viscous fluxes. The derivatives are calculated according to the method described by Peyret and Taylor [23]

$$\frac{\partial u}{\partial r} = \frac{1}{A}\oint u\,dz \quad (23)$$

$$\frac{\partial u}{\partial z} = -\frac{1}{A}\oint u\,dr \tag{24}$$

where A is the cell area. The integrals in equations (23) and (24) are approximated by finite sums giving:

$$\oint u\,dy = \sum_{f=1}^{4} u_f \Delta y_f \tag{25}$$

where the subscript f is a cell face index. This method of calculating derivatives automatically accounts for grid lines that are not parallel to the coordinate axes.

The integration regions used for evaluating the convective and viscous fluxes are different from one another (Fig. 4). Convective fluxes are calculated at nodes, resulting in cell centered flux balances (Fig. 4(a)), whereas viscous fluxes are defined at cell centers, resulting in node-centered flux balances (Fig. 4(b)). The entire scheme becomes node-centered by summing the convective flux balances from the four cells making up the 'node super-cell' (Fig. 4(c)).

The methodology described above defines a scheme that is formally second-order accurate. However, for forward time differencing, the scheme is unstable when viscous terms are small because the convective flux integration is equivalent to a centered difference approximation of the spatial derivatives appearing in equation (7). Artificial dissipation and a four-stage/time-stepping method described in the following sections are used to stabilize the numerical algorithm.

5. ARTIFICIAL DISSIPATION

The flux integration method described above is equivalent to a centered difference approximation of the flux vector derivatives in equation (16). Centered differencing of convective derivatives is unconditionally unstable when used with forward time stepping. Furthermore, the leading order error term of the modified differential equation that is actually being solved by the numerical method is proportional to the third derivative of the dependent variable. Odd order derivatives lead to wave dispersion phenomena resulting in oscillations near discontinuities, such as shock waves, and 'odd–even' decoupling of the numerical solution at neighboring node points. In the present study, 'artificial viscosity' is added to overcome odd–even decoupling.

The method of introducing artificial dissipation into the numerical solution algorithm used in this study is an extension and modification of methods described by Ni [24], Rizzi and Eriksson [25] and Powell [26]. The artificial dissipation has two components: a second-difference term that is turned on only at shocks, and a fourth difference term that is turned on where the turbulent viscosity is not high enough to damp odd–even decoupling. The fourth-difference term is $O(\Delta x^3)$ and therefore does not affect the formal solution accuracy. However, the second difference term degrades the solution accuracy to first order in shocks. This is typical of all 'shock-capturing' numerical schemes because the shock structures must be smeared out to at least the width of one grid cell for these numerical methods to be stable.

The fourth-difference operator is given by:

$$\mathbf{D}_4(\mathbf{U}) = \varepsilon_4 \mathbf{L}^2(\mathbf{U}) \tag{26}$$

where ε_4 is the fourth-difference artificial viscosity coefficient, $\mathbf{L}$ is an unweighted Laplacian operator, and $\mathbf{L}^2$ is the (unweighted) biharmonic operator. Away from the boundaries, the Laplacian is expressed as (see Fig. 5):

$$\mathbf{L}(\mathbf{U}) = \mathbf{U}_{SW}+\mathbf{U}_{SE}+\mathbf{U}_{NE}+\mathbf{U}_{NW} +2(\mathbf{U}_S+\mathbf{U}_E+\mathbf{U}_N+\mathbf{U}_W)-12\mathbf{U}. \tag{27}$$

The biharmonic operator appearing in equation (26) is simply calculated by applying the Laplacian operator (equation (27)) to the Laplacian of the state vector.

The second difference operator takes the form:

$$\mathbf{D}_2(\mathbf{U}) = \varepsilon_2 \bar{\mathbf{L}}(\mathbf{U}, \delta P) \tag{28}$$

where ε_2 is the second difference artificial viscosity coefficient (0.01–0.05), and $\bar{\mathbf{L}}$ is a modified Laplacian operator that uses a weighting function, δP, as follows:

$$\begin{aligned}\bar{\mathbf{L}}(\mathbf{U}, \delta P) = {} & (\mathbf{U}_{SW}-\mathbf{U})\delta P_{sw}+(\mathbf{U}_{SE}-\mathbf{U})\delta P_{se} \\ & +(\mathbf{U}_{NE}-\mathbf{U})\delta P_{ne}+(\mathbf{U}_{NW}-\mathbf{U})\delta P_{nw} \\ & +2(\mathbf{U}_S-\mathbf{U})\delta P_s+2(\mathbf{U}_E-\mathbf{U})\delta P_e \\ & +2(\mathbf{U}_N-\mathbf{U})\delta P_n+2(\mathbf{U}_W-\mathbf{U})\delta P_w.\end{aligned} \tag{29}$$

The weighting function is defined at node points by:

$$\delta P = \frac{\mathbf{L}(P)/P}{|\mathbf{L}(P)/P|_\infty} \tag{30}$$

where $|\ |_\infty$ denotes the maximum of the enclosed quantity over the entire solution domain. Values of

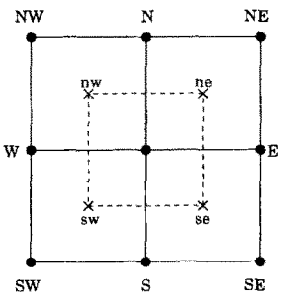

FIG. 5. Laplacian operator stensil (adapted from Powell [26]).

δP between nodes are obtained by taking the maximum, for example:

$$\delta P_{sw} = \max[\delta P, \delta P_{SW}]. \quad (31)$$

Boundary values of δP are set equal to zero. The use of the pressure switch given by equation (30) as a weighting function allows the algorithm to detect when shocks occur and automatically add second difference smoothing terms only in these regions. This is done in an attempt to use the minimum amount of smoothing possible for stable shock capturing.

Numerical experiments conducted during the present study indicate that the fourth-difference artificial dissipation expressed by equation (26) must be turned off in shocks, high turbulent viscosity regions, and in the boundary layer along the spalling rock surface in order to obtain solutions that are independent of the fourth difference artificial dissipation coefficient. The method used to automatically switch off the fourth difference artificial dissipation in the regions described above is expressed by:

$$\varepsilon_4^0 = \max\left[\varepsilon_4^0 - \varepsilon_2 \delta P - 3\left(\frac{(\mu_t)}{Re_r}\right), 0\right] \quad (32)$$

where ε_4^0 = user specified fourth difference damping coefficient (≈ 0.001). In addition, the total artificial dissipation was linearly reduced to zero across the outer region of the boundary layer by setting:

$$D_{bl}(\mathbf{U}) = \mathbf{D}(\mathbf{U})(y/R_{noz}) \quad (33)$$

where $D_{bl}(\mathbf{U})$ = total (second plus fourth difference) artificial dissipation in the boundary layer, and y = distance from the rock surface.

The second and fourth difference contributions are combined in the following way:

$$\mathbf{D}(\mathbf{U}) = \mathbf{D}_2(\mathbf{U}) - \mathbf{D}_4(\mathbf{U}) \quad (34)$$

and then added to the right-hand side of equation (16). The next section describes the numerical time integration method used to achieve the steady-state solution of equation (16).

6. TEMPORAL DISCRETIZATION

Equation (16) represents a coupled set of semi-discrete, non-linear equations describing the time rate of change of the state vector, $\mathbf{U}$. A multistage scheme is used to integrate these equations to steady state. The method is given by Jameson [27]:

$$\begin{aligned}
\mathbf{U}^1 &= \mathbf{U}^n - \alpha_1(\Delta t)(\mathbf{R}^n - \mathbf{D}^n)\\
\mathbf{U}^2 &= \mathbf{U}^n - \alpha_2(\Delta t)(\mathbf{R}^1 - \mathbf{D}^n)\\
\mathbf{U}^3 &= \mathbf{U}^n - \alpha_3(\Delta t)(\mathbf{R}^2 - \mathbf{D}^n)\\
\mathbf{U}^4 &= \mathbf{U}^n - \alpha_4(\Delta t)(\mathbf{R}^3 - \mathbf{D}^n)\\
\mathbf{U}^{n+1} &= \mathbf{U}^4
\end{aligned} \quad (35)$$

where $\alpha_1 = 0.25$; $\alpha_2 = 0.33$; $\alpha_3 = 0.50$; $\alpha_4 = 1.0$, $\mathbf{R}^k$ = the residual representing the spatially discretized form of equation (16) evaluated after stage 'k', $\mathbf{D}^n$ = artificial dissipation evaluated after stage n, and Δt = time step.

Computational efficiency is achieved by evaluating the physical and artificial dissipation terms during only the first stage.

7. SOLUTION OF TURBULENCE TRANSPORT EQUATIONS

The k–ε model equations given by equations (9) and (10) are of the same form as those in equation (7). Therefore, the convective, diffusive, and artificial dissipation terms are discretized as detailed in Sections 4–6. However, the turbulent kinetic energy production and dissipation terms are treated implicitly during each stage of the time integration procedure in order to improve numerical stability. The discrete, implicit forms of the turbulence transport equations are given by:

$$(\rho k)^{k+1} = (\rho k)^{k+1/2} - \alpha_k CFL(\rho\varepsilon)^{k+1} + \alpha_k CFL(P_k)^{k+1/2} \quad (36)$$

$$(\rho\varepsilon)^{k+1} = (\rho\varepsilon)^{k+1/2} + \alpha_k(CFL)(C_1)P_k\left(\frac{\rho\varepsilon}{\rho k}\right)^{k+1} - \alpha_k(CFL)C_2\left(\frac{(\rho\varepsilon)^2}{\rho k}\right)^{k+1} \quad (37)$$

where the superscript $k+1/2$ implies that the values have already been updated to account for the convective, diffusive, and artificial dissipation flux balances calculated at stage k, and CFL is the Courant–Friedrichs–Lewy number ($a\Delta t/\Delta x$).

Equations (36) and (37) are manipulated to yield an expression for the value of $(\rho\varepsilon)$ at stage $k+1$:

$$(\rho\varepsilon)^{k+1} = \frac{A_2 + \sqrt{(A_2^2 - 4A_1A_3)}}{2A_1} \quad (38)$$

where

$$A_1 = \alpha_k CFL(C_2 - 1),$$

$$A_2 = (\rho k)^{k+1/2} + \alpha_k CFL(\rho\varepsilon)^{k+1/2} - \alpha_k(CFL)C_1P_k^{k+1/2},$$

and

$$A_3 = -[(\rho\varepsilon)(\rho k)]^{k+1/2}.$$

The solution to equation (38) is substituted back into equation (36) to determine the updated value of (ρk). After solving equations (37) and (38), values of the turbulent viscosity are updated at all node points using equation (8). As discussed earlier, μ_t relates the strain rate to the apparent viscous stresses throughout the turbulent flow field.

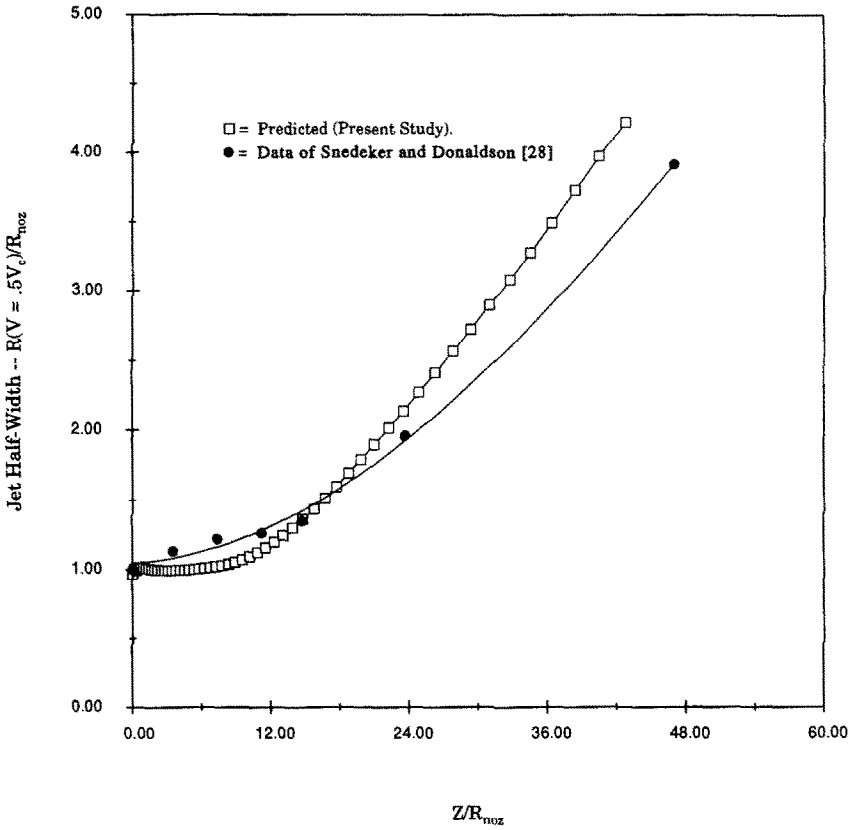

FIG. 6. Radial spread of a subsonic jet—comparison between experimental data and model predictions.

8. SOLVER VALIDATION

The accuracy of the code used in this study is illustrated by comparing simulation results for subsonic and supersonic free jets with experimental data obtained by Snedeker and Donaldson [28], Wyganski and Fiedler [29], and Rodi [30]. In addition, comparison is made with predictions of other researchers who used k–ε turbulence models for predicting subsonic jets.

The rate of spread of a turbulent jet is governed by the rate of entrainment of surrounding fluid through the action of turbulent diffusion at the jet boundary [31]. Therefore, comparing predicted and experimental jet spreading rates provides a test of the combined ability of the turbulence model and numerical method to accurately represent flow fields similar to those that occur near the nozzle outlet during spallation drilling.

Subsonic free jet. Plots of simulated and experimental [28] jet half-width vs downstream distance for a subsonic turbulent free jet exhausting into stagnant surroundings are shown in Fig. 6. Jet half-width is defined for a given downstream distance as the radius at which the axial velocity equals one-half of the maximum axial jet velocity. Both jet half-width and downstream distance are non-dimensionalized with nozzle radius. The nozzle outlet conditions and numerical parameters used for modeling this flow-field are listed in Table 1.

The half-width of a free jet is known to grow linearly with downstream distance from the nozzle once the potential core has disappeared and self similarity of cross-stream velocity profiles has occurred [32]. In this case, self similarity is said to occur when plots of axial velocity, turbulence intensity, temperature, etc., non-dimensionalized with their respective centerline values vs radius, non-dimensionalized with the jet half-width, fall on the same curves regardless of the axial location. The slope of the line joining the jet half widths in the self similar region of the flow-field is defined as the spreading rate.

Table 1. Nozzle outlet conditions and modeling parameters for subsonic free jet

Parameter	Value
Nozzle Mach number (Ma)	0.52
Nozzle Reynolds number (Re_{noz})	129 200
Inlet turbulence intensity	0.5% of mean kinetic energy
C_1, C_2, C_3	1.42, 1.92, 3.13
CFL	1.0
ε_2^0, ε_4^0	0.0, 0.001

Table 2. Comparison of predicted round-jet spreading rates with measurements and predictions of other investigators

Experiment (Snedeker and Donaldson [28])	0.086
Experiment (Rodi [30], Wyganski and Fiedler [29])	0.087
Predicted-Reynolds stress closure (Launder & Morse [34])	0.136
Predicted-standard (Hanjalic and Launder [33])	0.115
Predicted-modified (Hanjalic and Launder [33])	0.098
Predicted-modified (this study)	0.100

Note: Spreading rate is defined as $\partial r_{1/2}/\partial z$ where $r_{1/2}$ = the radius at which the jet velocity equals one-half of the centerline value and z is axial distance measured from the nozzle outlet. In the self-similar jet region, the spreading rate is constant.

Table 2 contains a comparison of spreading rates obtained by several experimenters [28–30] with predictions of other workers and with predictions made during the present study. The level of error in the experimental results is unknown but the good agreement obtained between the results for the three experimental studies cited indicates that the error is probably less than 1%. The present prediction (shown as 'this study' in Table 2) uses the 'modified' turbulent dissipation equation of Hanjalic and Launder [33] and is about 15% too high when compared to the experiments. In the 'modified' k–ε model, a separate constant (C_3) is used to multiply the terms responsible for turbulence production by normal stress components in the transport equation for the dissipation rate of turbulent kinetic energy. This modified form contrasts to the 'standard' k–ε model which does not properly account for the relatively high normal stresses that occur in round turbulent jets and, therefore, overpredicts the spreading rate by about 30–35% (Table 2). Both the standard and the modified k–ε models predict spreading rates for planar jets to within approximately 2% of experimentally measured values.

A comparison between predicted and experimental [30] non-dimensional turbulent kinetic energy profiles in the self similar region of the jet is shown in Fig. 7. In this case, the turbulent kinetic energy (k) is scaled with centerline velocity (U_c) squared and radial position is scaled with jet half width ($r_{1/2}$). The 8–10% under-prediction of centerline turbulence levels is comparable with the results of Hanjalic and Launder [33].

Supersonic free-jet. Figure 8 is a comparison of predicted jet half-widths with experimental values [28] for a sonic ($Ma = 1$), highly underexpanded ($P_{jet}/P_{amb} = 3.57$) jet exhausting into stagnant surroundings. Other parameters are listed in Table 3.

Experimental errors are estimated as $\pm 5\%$. The terminal spreading rate is overpredicted by about the same percentage in this case as for the subsonic case. Furthermore, the predicted supersonic core length

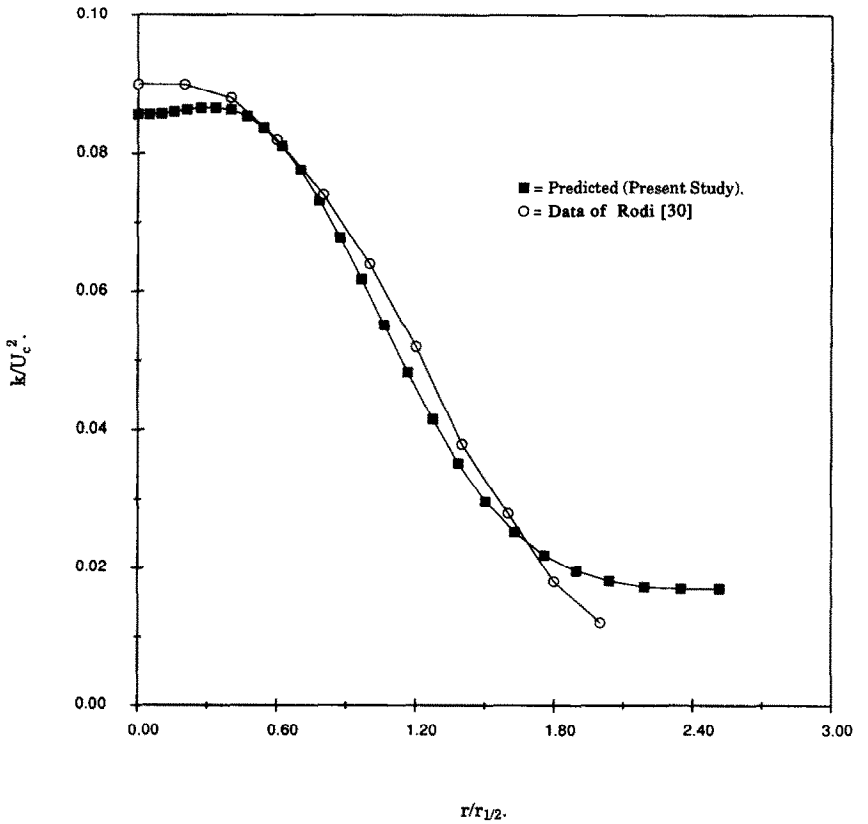

FIG. 7. Predicted and experimental turbulent kinetic energy profiles (specifications given in Table 2).

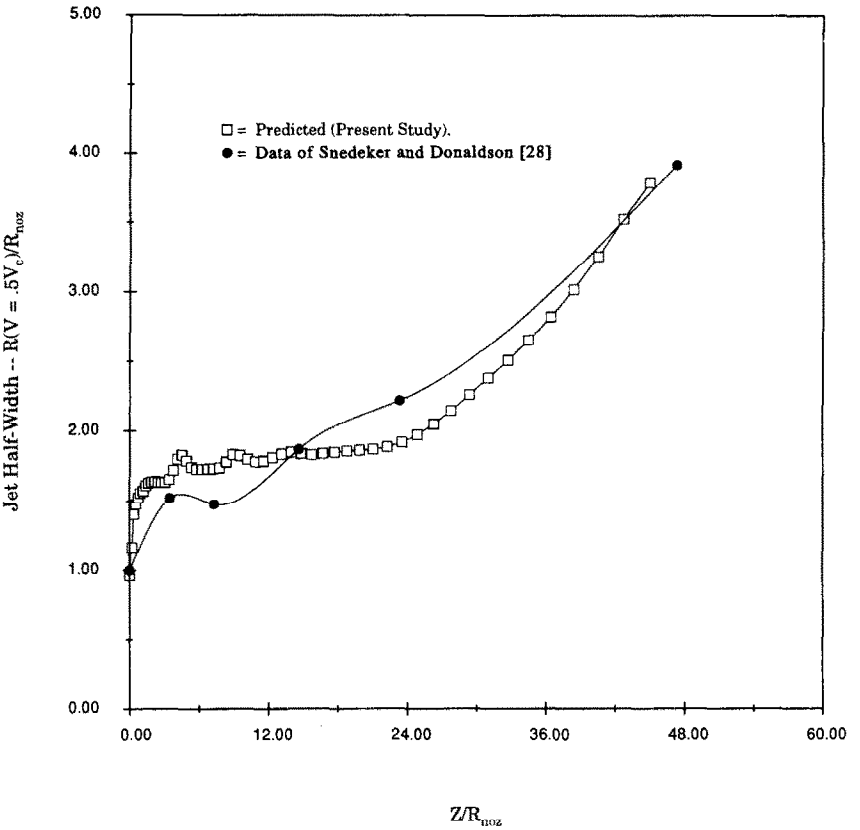

FIG. 8. Radial spread of a supersonic jet—comparison between experimental data and model predictions.

(the last downstream point at which the centerline $Ma \geqslant 1$) is 36 nozzle radii (Fig. 9), as compared to experimental values of about 40–44 nozzle radii [28]. Correct prediction of the supersonic core length is important because it determines whether or not a normal stand-off shock occurs in the impinging flow-field during thermal spallation drilling.

Approximately three shock diamonds, corresponding to pairs of extrema in the Ma vs Y curve, are predicted at the nozzle outlet as the high inlet pressure adjusts to the ambient pressure (Fig. 9). The first of these shocks results in a Mach number less than one, implying that a 'Mach disk' forms normal to the mean flow direction. The second and third shocks are predicted to be oblique, although the data of Snedeker and Donaldson [28] indicate that the second one is also a Mach disk. Reducing the second difference artificial dissipation coefficient in the present scheme results in correct prediction of the second normal Mach disk but destabilizes the code by allowing small oscillations of the shock structure. Supersonic core length and jet-spreading rate were affected by less than 4% by changing the artificial dissipation level.

Table 3. Nozzle outlet conditions and modeling parameters for supersonic free jet

Parameter	Value
Nozzle Mach number (Ma)	1.0
Nozzle Reynolds number (Re_D)	600 000
Inlet turbulence intensity	5% of mean kinetic energy
C_1, C_2, C_3	1.42, 1.92, 3.13
CFL	1.0
ε_2^0, ε_4^0	0.01, 0.001
P_{jet}/P_{amb}	3.57

Free-jet predictions using the standard form of the k–ε model have also been conducted during this study. Although not shown, the resulting subsonic jet spreading rates are about 2% lower than those obtained by Hanjalic and Launder [33] using the same model (see Table 2). Calculations of the supersonic case resulted in a core length of 32 nozzle radii and a terminal spreading rate approximately equal to that given by Hanjalic and Launder's subsonic prediction (standard model).

The modified value of C_3 in the validation work described above was used to investigate variations in prediction accuracy possible for relatively minor changes to the modeling constants and to confirm that similar levels of accuracy could be obtained using the flow-field solver implemented in the present study as those obtained previously by other workers. Preliminary simulation runs were conducted using

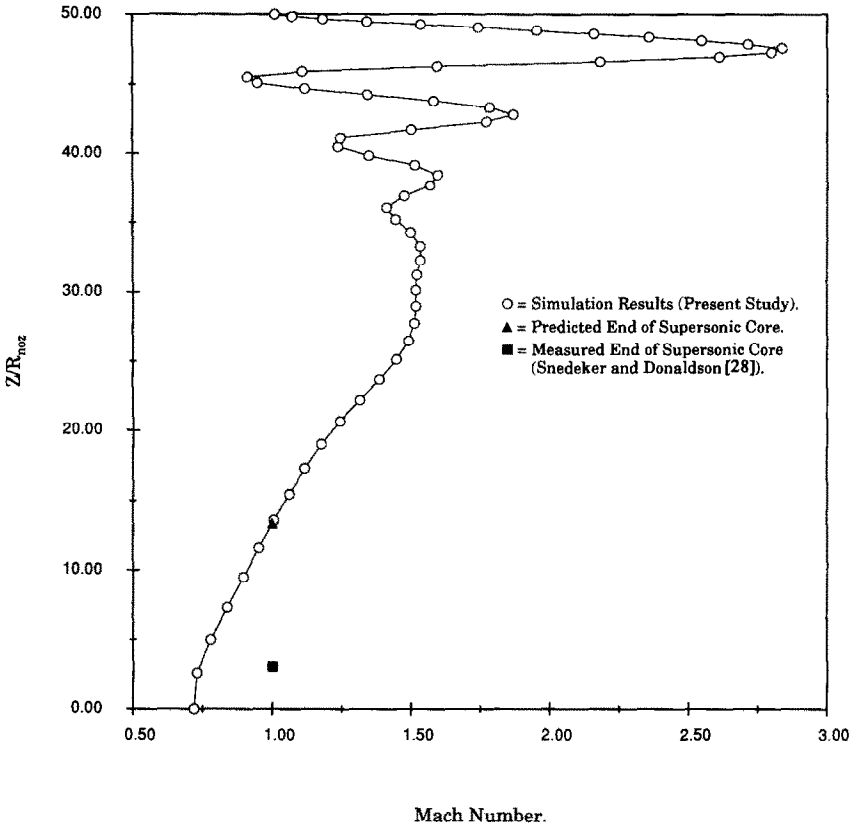

FIG. 9. Centerline Mach number as a function of distance from the nozzle outlet.

'standard' and 'modified' k–ε models for predicting impinging jet flow fields similar to those that occur during thermal spallation drilling and revealed that the increased sensitivity to normal strain rates of the modified model leads to nonphysical results near the stagnation point. Predicted turbulent viscosity values approach zero because of the higher predicted levels of the turbulence dissipation rate. A large flow recirculation zone forms starting at the stagnation point and having a radius of approximately six nozzle radii. These results conflict with experimental observations made by Snedeker and Donaldson [28] for impinging supersonic jets. Moreover, predicted penetration rates were two orders of magnitude less than those routinely observed using thermal spallation drilling.

The standard k–ε model did not predict the anomalous recirculation zone described above, and predicted heat transfer rates and spatial heat transfer distributions consistent with those observed in practice for both subsonic and supersonic jets at moderate stand-off distances and pressures. Furthermore, the standard k–ε model has been extensively tested by other researchers and the various modeling parameters have been more firmly established than the modified constants of Hanjalic and Launder [33]. Therefore, the standard k–ε model was used for all thermal spallation simulations reported in this paper. The maximum accuracy that is expected to be achievable for jet-spreading rate and supersonic core length is approximately $\pm 35\%$, corresponding to the errors for the 'standard' model results given in Table 2. Since the behavior of the wall jet and corresponding heat transfer to the rock surface is heavily influenced by the impinging jet flow field, similar, or worse, accuracy should be expected for the overall simulation results.

9. GRID GENERATION

Grid generation is broken down into two steps in this study: determination of an initial grid with appropriate point clustering in high gradient regions and smoothing of the grid using an elliptic equation set to equalize grid spacings and force the cell edges closer to orthogonality with one another. The elliptic grid generation procedure described by Steger and Sorenson [35] was used to smooth the initial grid. A typical example of a final grid is illustrated in Fig. 10.

10. BOUNDARY MOVEMENT ALGORITHM

The component of the penetration rate that is parallel to the drill axis (V_{dr}) must be the same at steady-state conditions for all points along the spalling rock surface. Equation (2) accounts for this effect with the cos (θ) term. V_{dr} is calculated as an average of pre-

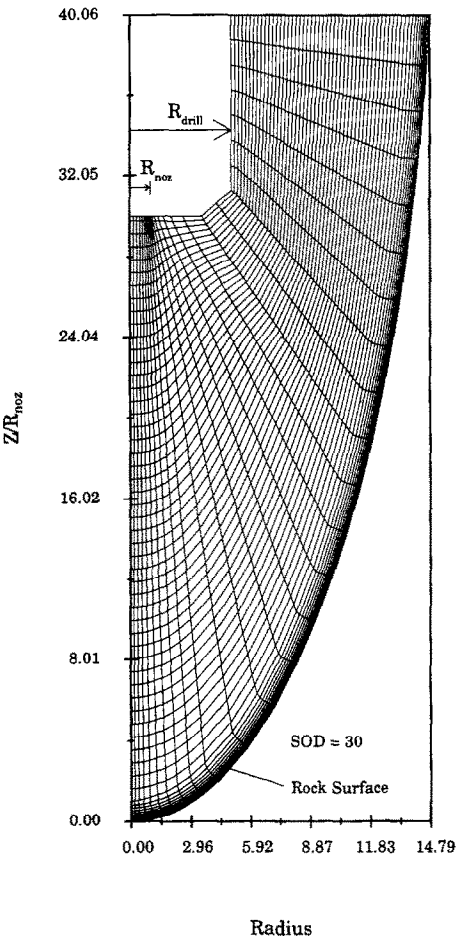

FIG. 10. Smoothed computational grid.

dicted penetration rates for all points from a radius of one-half nozzle diameters to the point where $\theta = 45°$.

The average of the drilling velocities predicted for the previous and current boundary heat flux profiles is used to determine the movement necessary to force self-consistency. The equation used is:

$$U_{\mathrm{dr},i} = \frac{1}{2}\left(U_{\mathrm{dr},i}^{\mathrm{old}} + \frac{Q_i}{(\rho C_p)_r (T_{\mathrm{s},i} - T_{\mathrm{r},0})}\right) \quad (39)$$

where $U_{\mathrm{dr},i}^{\mathrm{old}}$ = previous predicted value of penetration rate at location 'i'.

The updated boundary angle at each location is calculated by averaging the current value with that predicted by the local penetration rate:

$$\cos(\theta_i) = 0.5(\cos(\theta_i)^{\mathrm{old}} + U_{\mathrm{dr},i}/V_{\mathrm{dr}}). \quad (40)$$

The non-dimensional ratio of the local excess to average penetration rate (R_{pr}) at each point on the surface is given by:

$$R_{\mathrm{pr},i} = U_{\mathrm{dr},i}/V_{\mathrm{dr}} - 1. \quad (41)$$

These values are smoothed by averaging each with the values from the two nearest neighboring boundary points so that 'wiggles' do not appear. The boundary movement is finally performed by using the smoothed values of R_{pr} giving:

$$r_i^{\mathrm{new}} = r_i^{\mathrm{old}} + \omega R_{\mathrm{pr},i} \sin(\theta) \quad (42)$$

$$z_i^{\mathrm{new}} = z_i^{\mathrm{old}} - \omega R_{\mathrm{pr},i} \cos(\theta) \quad (43)$$

where r_i and z_i are non-dimensional boundary coordinates, and ω = a user-defined acceleration parameter (≈ 2.0). R_{pr} is always set equal to zero at the centerline and the boundary is not allowed to move below $z = 0$ so that the stand-off distance cannot change during a simulation, since stand-off distance is considered an input parameter.

During most runs, the starting boundary shape was elliptical and the first steady-state solution was achieved after 1000–1500 iterations. Typical requirements for the remainder of the simulation were: less than 1000 iterations to achieve a steady-state flow field at each fixed boundary position, and 50–70 boundary movements to reach the final hole shape. Convergence of the hole shape was observed to occur when the predicted variations were less than 0.5 nozzle radii. Typically, about one hour of CPU time on a Cray-XMP computer was required for convergence at each stand-off distance and set of conditions.

11. SIMULATION RESULTS

Predicting penetration rates and hole radii depends upon predicting the steady-state flow-field for each hole geometry, and, after the required number of boundary adjustments, a steady-state hole geometry for each specified set of torch operating conditions. Each flow field was assumed to have converged when an averaged value of the Stanton number (St) varied by less than 0.5% per 1000 iterations. Predicted hole shape usually oscillated toward a steady-state value and convergence was assumed when the amplitude of the oscillations in the hole radius was less than 0.25 nozzle radii.

Computer simulation runs were conducted for three sets of modeling assumptions: the basic solver, as outlined above; the basic solver with a heat capacity that varies with gas temperature, and the basic solver with a variable heat capacity and mass injection at the spalling surface to represent the momentum deficit introduced into the boundary layer by spall liberation. The effect of each of these modeling methods is illustrated in the plot of St vs non-dimensional hole radius in Fig. 11.

The most important improvements in the basic solver algorithm used in this study over the approach developed in 1986 by Rauenzahn [6] are second order accurate advection and node point clustering in high gradient regions. These improvements should result in less numerically-induced smearing of flow-field gradients and correspondingly higher values for wall heat fluxes and shear stresses. In Fig. 11, the curve generated in the present study is seen to be higher

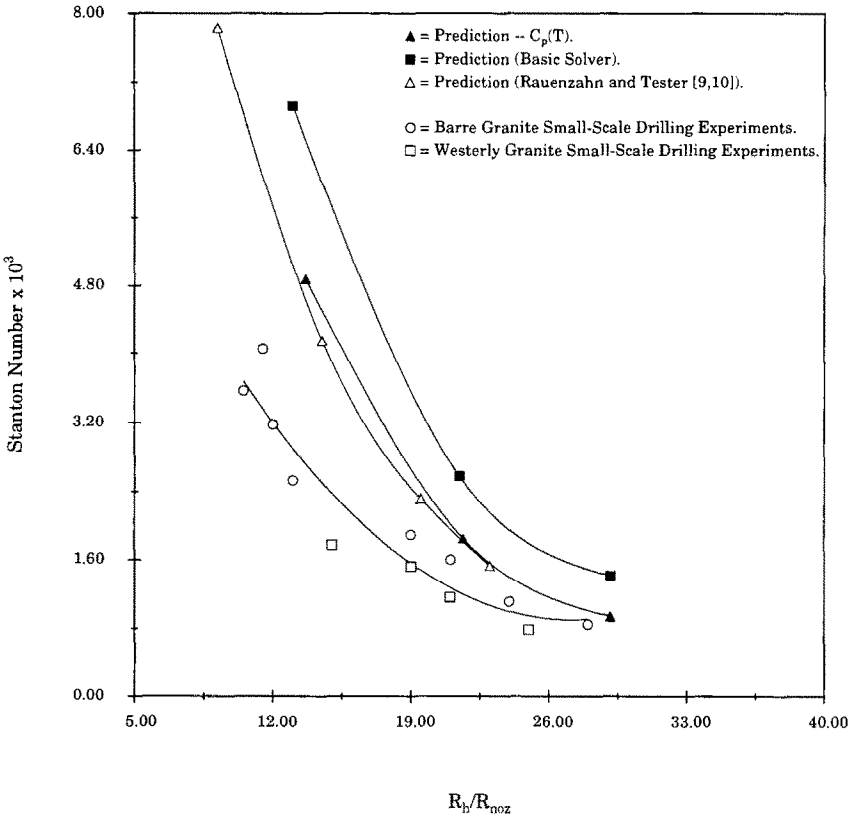

FIG. 11. Stanton number vs hole radius—illustration of effects of variable heat capacity on simulation accuracy.

than the results reported by Rauenzahn and Tester [9, 10], and both predicted curves are higher than the experimental results.

In the basic solver, the value of the heat capacity is set equal to the inlet value throughout the flow-field. In reality, the heat capacity decreases at lower gas temperatures resulting in lower heat capacities near the rock wall than at the nozzle. A lower heat capacity results in a proportionally lower turbulent thermal conductivity (λ_t) because the turbulent Prandtl number ($Pr_t = \mu_t C_p/\lambda_t$) is assumed constant at 0.86. The results for the variable heat capacity case illustrated in Fig. 11 indicate that the predicted Stanton numbers decrease by approximately 30% compared to the values predicted using the basic solver. However, the results are still about 1.5 times higher than experimentally observed Stanton numbers.

Roberts *et al.* [36] observed that solids liberation from a surface changes the turbulent boundary layer structure and reduces heat transfer rates to the surface. In the present study, spall liberation from the rock surface is approximated, perhaps crudely, by assuming that it is similar to transpiration blowing. The modeling is implemented by applying blowing boundary conditions to the convective terms of the far-field conservation equations. Therefore, at the rock boundary, the mass flux normal to the surface is set equal to the main flux determined by the local drilling rate:

$$(\rho V) = (\rho_r U_{dr}). \tag{44}$$

Recall that U_{dr} is determined from the calculated heat flux through equation (1), assuming that $\Delta H_{pt} \approx 0$. Heat fluxes and viscous stresses are calculated using the traditional wall functions (equations (13) and (14)) without modifications for the cross-stream variations in shear stress and heat flux that would occur during true transpirational blowing since the frequency of spall ejection is low relative to the characteristic time for the hot gases to advect along the rock surface and out of the actively spalling region.

Simulation results including variable heat capacity and mass injection are plotted in Fig. 12 and are within 5% of experimental Stanton number and hole radius measurements. Adding a variable heat capacity and approximating mass injection due to spall liberation each made about the same contribution toward diminishing the discrepancy between experimental data and results predicted by the basic solver.

12. CONCLUSIONS AND RECOMMENDATIONS

Despite the agreement between predicted and experimental results, an accurate description of the

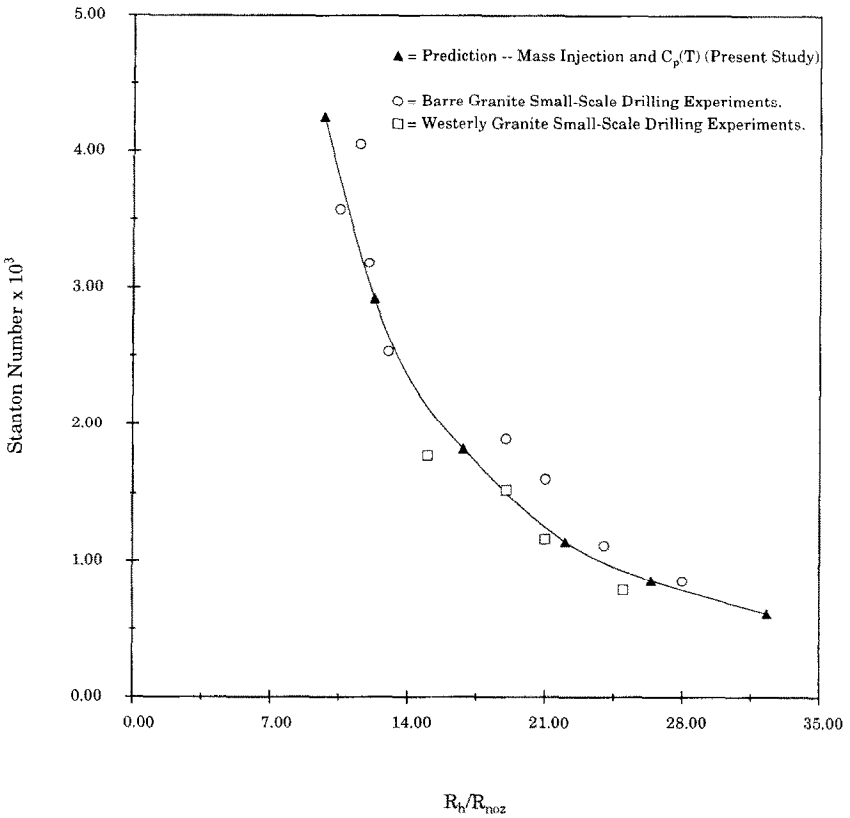

FIG. 12. Stanton number vs hole radius—comparison of experimental results with predictions made using variable heat capacity and mass injection.

boundary layer velocity and temperature profiles is necessary to validate the modeling employed in the present study, especially with the approximations made in modeling the influence of spall liberation on heat transfer. The present approach should be regarded as an attempt at placing bounds on the potential influence of spall liberation on the transport phenomena occurring during spallation drilling. The good agreement between predictions and experiments could simply be the result of fortuitous cancellation of errors. Future experimental and theoretical and theoretical studies of the physical interactions between gases and solids within turbulent boundary layers, for example large eddy simulation, are necessary before more detailed modeling can be justified for representing the flow field that exists during thermal spallation drilling.

The general behavior of the predicted Stanton number vs hole radius is quantitatively characterized using either the upwind differencing method of Rauenzahn [6], or the second-order accurate method employed in the present study. Using the second-order numerical method for the base solver resulted in about 30% higher values of predicted Stanton numbers than those reported earlier by Rauenzahn and Tester [9, 10]. Including the effect of the temperature variation on the gas heat capacity reduced predicted Stanton numbers by approximately 30% relative to the base solver, accounting for some of the discrepancy between predicted and experimental Stanton numbers. Approximating the effects of spall liberation from the rock surface on heat transfer rates as continuous transpiration blowing further reduced predicted Stanton numbers by 35%. The combination of all these effects resulted in excellent agreement (within 5%) with experimental results, suggesting that the mass-injection effect upon the boundary layer should be investigated further.

Future efforts should focus on expanding the spallation drilling data base, focussing attention on measuring those quantities that are necessary for validating computational models. The data base could be expanded by performing laboratory drilling experiments varying P_{jet}, T_{jet}, Re_{jet}, and Ma_{jet}.

To improve the flexibility of the computational model for predicting alternate geometries (e.g. cavity formation), an unstructured methodology for grid generation and flow model implementation should be considered. To increase understanding of the influence of spall entrainment on near-wall transport phenomena, heat flux and turbulence structure measurements on a simplified flow geometry (e.g. a flat plate) with intermittent solids injection should be performed. Finally, to rapidly estimate penetration rate and

hole geometry trends during thermal spallation drilling, a lumped parameter model should be formulated using insight gained from numerical modeling and field experiments.

Acknowledgements—The authors would like to thank Rick Rauenzahn, Robert Potter, Judson Baron, Pretinder Virk, and Kenneth Smith for their useful comments and suggestions during the course of this work. CRAY computer time was provided by Los Alamos National Laboratory and Sandia National Laboratories provided partial support of this project. The Natural Sciences and Engineering Research Council of Canada is also gratefully acknowledged for providing partial fellowship support to one of the authors (MAW). The efforts of the anonymous reviewers of the paper in pointing out areas for improvement are also acknowledged.

REFERENCES

1. J. A. Browning, Flame-jet drilling in conway, N.H. granite, Unpublished report of work done under Univ. of California order number 4-L10-2889R-1 (1981).
2. R. E. Williams, T. Dey, R. M. Rauenzahn, R. M. Kranz, J. W. Tester, R. Potter and H. Murphy, Advancements in thermal spallation drilling technology, Los Alamos National Laboratory Report LA-11391-MS, Los Alamos, NM (1988).
3. H. C. H. Armstead and J. W. Tester, *Heat Mining*. E. & F.N. Spon, London (1987).
4. J. W. Tester and H. J. Herzog, The economics of heat mining: an analysis of design options and performance requirements of hot dry rock (HDR) geothermal power systems, *Energy Systems and Policy* **15**(1), 33–63 (1992).
5. R. E. Williams, F. E. Beck and R. M. Potter, Thermal spallation drilling research report, Subcontract No. 9-X68-5616R-1 between Los Alamos National Laboratory and New Mexico Institute of Mining and Technology (1991).
6. R. M. Rauenzahn, Analysis of the rock mechanics and gas dynamics of flame-jet thermal spallation drilling, Ph.D. Thesis, Massachusetts Institute of Technology (1986).
7. R. M. Rauenzahn and J. W. Tester, Flame-jet induced thermal spallation as a method of rapid drilling and cavity formation, *Proc. 60th Assn. Tech. Conf. and Exhibition*, Soc. Petrol. Eng. Paper 14331, Las Vegas, NV (1985).
8. R. M. Rauenzahn and J. W. Tester, Rock failure mechanisms of flame-jet thermal spallation drilling: theory and experimental testing, *Int. J. Rock Mech. Min. Sci.* **26**(5), 381–399 (1989).
9. R. M. Rauenzahn and J. W. Tester, Numerical simulation and field testing of flame-jet thermal spallation drilling—Part I. Model development, *Int. J. Heat Mass Transfer* **34**, 795–808 (1991).
10. R. M. Rauenzahn and J. W. Tester, Numerical simulation and field testing of flame-jet thermal spallation drilling—Part II. Experimental verification, *Int. J. Heat Mass Transfer* **34**, 809–818 (1991).
11. J. A. Browning, W. B. Horton and H. L. Hartman, Recent advances in flame-jet working of minerals, *7th Symp. Rock Mech.*, Pennsylvania State University (1965).
12. T. N. Dey, More on spallation theory, Los Alamos National Laboratory Internal Memorandum No. ESS-3-286-84 (1984).
13. M. A. Wilkinson and J. W. Tester, Experimental measurement of surface temperatures during flame-jet induced thermal spallation, *Rock Mech. Rock Engng* **26**(1), 29–62 (1993).
14. O. Reynolds, On the dynamical theory of incompressible viscous fluids and the determination of the criterion, *Phil. Trans. Roy. Soc.* A **186**, 123–164 (1895).
15. J. Boussinesq, Essai sur la theorie des eaux courantes, *Mem. Prestes Acad. Sci.* **23**, 46 (1877).
16. B. E. Launder and D. B. Spalding, The numerical calculation of turbulent flows, *Comput. Methods Appl. Engng* **3**, 269–289 (1974).
17. W. P. Jones and B. E. Launder, The prediction of laminarization with a two-equation model of turbulence, *Int. J. Heat Mass Transfer* **15**, 303–314 (1972).
18. J. R. Viegas and M. W. Rubeson, Wall-function boundary conditions in the solution of the Navier–Stokes equations for complex compressible flows, Paper No. AIAA-83-1694 (1983).
19. L. Prandtl, Uber die ausgebildete Turbulenze, *ZAMM* **5**, 136–139 (1925).
20. D. F. Dipprey and R. H. Sabersky, Heat and momentum transfer in smooth and rough tubes at various Prandtl numbers, *Int. J. Heat Mass Transfer* **6**, 329–353 (1963).
21. M. A. Wilkinson, Computational modeling of the gas-phase transport phenomena and experimental investigation of surface temperature during flame-jet thermal spallation drilling, Ph.D. Thesis, Massachusetts Institute of Technology, Cambridge, MA (1989).
22. P. L. Roe, Error estimates for cell-vertex solution of compressible Euler equations, NASA CR-178235 (1987).
23. R. Peyret and T. D. Taylor, *Computational Methods for Fluid Flow*. Springer-Verlag, Berlin (1983).
24. R. H. Ni, A multiple grid scheme for solving the Euler equations, AIAA Paper 81-1025 (1981).
25. A. Rizzi and L. E. Eriksson, Computation of flow around wings based on the Euler equations, *J. Fluid Mech.* **148**, 45–71 (1984).
26. K. G. Powell, Vortical solutions of the conical Euler equations, Ph.D. Thesis, Massachusetts Institute of Technology (1988).
27. A. Jameson, A vertex based multigrid algorithm for three-dimensional compressible flow calculations, *ASME Symposium on Numerical Methods for Compressible Flow*, Annahiem (1986).
28. R. S. Snedeker and C. duP. Donaldson, Experiments on free and impinging underexpanded jets from a convergent nozzle, Aero. Res. Assoc. Princeton Report No. ARAP-63 (1964).
29. I. Wyganski and H. E. Fiedler, Some measurements in the self-preserving jet, *J. Fluid Mech.* **38**, 577–612 (1969).
30. W. Rodi, The prediction of free turbulent boundary layers by use of a two-equation model of turbulence, Ph.D. Thesis, University of London (1972).
31. H. Schlichting, *Boundary Layer Theory* (7th Edn). McGraw-Hill, New York (1979).
32. J. O. Hinze, *Turbulence* (2nd Edn). McGraw-Hill, New York (1975).
33. K. Hanjalic and B. E. Launder, Sensitizing the dissipation equation to irrotational strains, *J. Fluids Engng* **102**, 34–40 (1981).
34. B. E. Launder and A. Morse, Numerical prediction of axisymmetric free shear flows with a Reynolds stress closure. In *Turbulent Shear Flows I*. Springer-Verlag, New York (1979).
35. J. L. Steger and R. L. Sorenson, Automatic mesh point clustering near a boundary in grid generation with elliptic partial differential equations, *J. Comput. Phys.* **33**, 405–410 (1979).
36. G. T. Roberts, R. A. East and N. H. Pratt, Surface heat transfer measurements from a turbulent, dusty boundary layer, *Proc. 14th Int. Symp. on Shock Tubes and Shock Waves*, pp. 455–462, Sydney, Australia (1983).